Bubble Cutting by Cylinder – Elimination of Wettability Effects by a Separating Liquid Film

Shuo Wang[1,2], Patrick Rohlfs[1], Marion Börnhorst[1], Andrea Schillaci[1,3], Holger Marschall[4], Olaf Deutschmann[1,5], and Martin Wörner[5,*]

DOI: 10.1002/cite.202100145

Supporting Information available online

Dedicated to Prof. Dr. Thomas Hirth on the occasion of his 60th birthday

Experiments and simulations are presented for the interaction of single bubbles rising in a viscous liquid against a horizontal cylinder (Ø = 4 mm) of varying wettability. The slide-off of small and the cutting of larger bubbles into two daughter bubbles observed in the experiment are reproduced by phase-field simulations. It is shown that in the entire process bubble and cylinder are separated by a liquid film, which eliminates any influence of cylinder wettability. Before the mother bubble splits, a thinning gas thread develops below the cylinder. The rupture of this gas thread can lead to a different number of satellite bubbles depending on the conditions.

Keywords: Bubble columns, Bubble fragmentation, Multiphase flows, Phase-field method

Received: July 29, 2021; *revised:* November 03, 2021; *accepted:* January 11, 2022

1 Introduction

One of the main challenges facing the chemical industry is the transition to sustainable operations. Consequently, the use of renewable raw materials as new feedstock has gained considerable attention [1]. Strategies for the intensified use of bio-based products are developed to substitute fossil and conventional resources. The increasing interest in renewable fuels has drawn attention to the production of liquid hydrocarbon fuels from biomass [2] via Fischer-Tropsch synthesis [3] as final step. Fischer-Tropsch synthesis is often performed in bubble column reactors. To foster the use of renewable raw materials in chemical industry, innovative solutions are required for raw material production, biomass treatment, and process engineering. Furthermore, besides improved catalysts, a deeper understanding of the underlying physico-chemical processes is required.

Most industrial bubble column reactors require the utilization of internal structures for heat transfer and/or for controlling the flow structures and back mixing in the system [4, 5]. Furthermore, internals may serve to fragment bubbles, thereby increasing interfacial area and mass transfer. For catalyzed three-phase reactions, bubble columns staged with woven fibrous materials have been suggested in this context [6, 7]. In comparison to conventional multistage bubble columns, the trays are made from woven fibrous catalytic layers [8]. The fiber networks divide the bubble column into two zones – a bubble zone and a reaction zone (Fig. 1). In the bubble zone, there is a radial mixing of the two phases and saturation of the liquid phase; in the reaction zone, gas and liquid react by interaction with the catalytically coated fibers.

[1]Shuo Wang, Patrick Rohlfs, Dr. Marion Börnhorst, Andrea Schillaci, Prof. Olaf Deutschmann
Karlsruhe Institute of Technology (KIT), Institute for Chemical Technology and Polymer Chemistry, Engesserstraße 20, 76131 Karlsruhe, Germany.

[2]Shuo Wang
Current address: Department of Applied Physics, Eindhoven University of Technology, Postbus 513, 5600 MB Eindhoven, The Netherlands.

[3]Andrea Schillaci
Current address: Department of Aerospace Sciences and Technologies, Politecnico di Milano, via La Masa 34, 20156 Milano, Italy.

[4]Dr. Holger Marschall
Technical University Darmstadt, Computational Multiphase Flows, Alarich-Weiss-Straße 10, 64287 Darmstadt, Germany.

[5]Prof. Olaf Deutschmann, Dr. Martin Wörner
martin.woerner@kit.edu
Karlsruhe Institute of Technology (KIT), Institute of Catalysis Research and Technology, Engesserstraße 20, 76131 Karlsruhe, Germany.

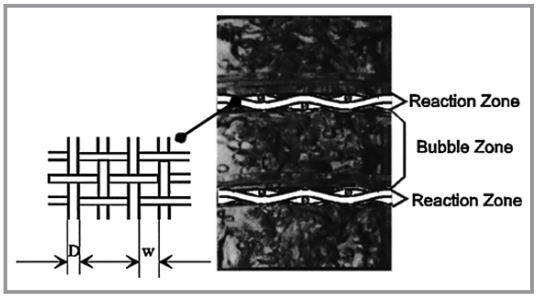

Figure 1. Bubble column staged with structured fibrous catalysts. Reprinted with permission from [7]. Copyright (2001) American Chemical Society.

For fiber networks as well as conventional internals of bubble column reactors, the understanding of the interaction of the bubbles with the structure is of interest. In the ERC starting investor grant "Cutting Bubbles", experiments and numerical simulations for various scales and flow conditions have been performed to study the interaction of bubbles with wire meshes [9–12] and single wires/cylinders [13, 14]. However, the influence of structure/wire wettability was not investigated and the contact angle was not taken into account in numerical simulations. Later, Cai et al. [15] recalculated selected cases from [13, 14] with a phase-field method considering different contact angles (θ) ranging from hydrophilic conditions with $\theta = 30°$ and 60° to neutral ($\theta = 90°$). For the two lower contact angles, the numerical split outcome in [15] in form of two daughter bubbles agreed reasonably well with experimental observations [13, 14], while results for 90° deviated. For the splitting process itself, the numerical results in [15] indicated a notable influence of contact angle. However, the authors stressed that there is no validation as detailed experiments for cylinders of varying wettability are lacking in literature. Also, in a recent experimental and theoretical study of bubble collisions on parallel arranged fibers, potential effects of fiber wettability are not addressed [16].

This paper studies in detail how far the interaction between a rising bubble and a horizontal cylinder depends on surface wettability. To this end, experiments and numerical simulations with single bubbles interacting with cylinders exhibiting different contact angles are performed. Here, cylinders of fixed diameter (4 mm) made from two materials (glass, steel) are considered in combination with bubbles of different volumes rising in a viscous liquid. The experiments provide images recorded by a high-speed camera from front views along the cylinder axis. They are complemented by refined numerical simulations with a phase-field method for widely varying contact angles, allowing for visualization from below which gives new insights in the bubble splitting process.

2 Experiment

2.1 Experimental Set Up

The experimental set up shown in Fig. 2 is adopted from [13, 14]. It consists of an optically accessible acrylic glass container (cross section $200 \times 200\,mm^2$, height 500 mm) which is partially filled with glycerol-water solution containing 90 wt % glycerol. At height 180 mm, a cylinder is placed horizontally in a hole of a vertical acrylic glass plate. At the bottom of the tank, a fixed volume of air can be injected through an inlet using a syringe. The air is collected below a rotatable spoon attached above the inlet. The air is allowed to coalesce forming a single bubble, which can be released by turning the spoon. Here, bubbles with volumes of 50, 250, and 500 µL are investigated. The high viscosity of the glycerol-water solution ensures a rectilinear rise so that the bubble likely hits the cylinder. The cylinder is either a hollow glass tube (contact angle $\theta \approx 40°$) or made of massive stainless steel ($\theta \approx 60°$). In both cases, the cylinder has a diameter of $d_{cyl} = 4$ mm and a length of 80 mm. Results of further experiments with cylinders of different diameter and wettability can be found in [17].

2.2 Image Recording

The rising bubble and its interaction with the horizontal cylinder are recorded by a high-speed camera (PCO 1200hs, 60 mm F-mount objective) using backlight illumination (Veritaslight Constellation 120E LED Spotlight). The recording was set at a frame rate of 1000 Hz, focused at a domain of $40 \times 32\,mm^2$ with a resolution of $32\,pixel\,mm^{-1}$. Dimensions are evaluated with the software ImageJ. The recorded image sequences show the 2D projection of a rising bubble, which is cut by a horizontal cylinder. Rising bubbles are assumed to have an axisymmetrical shape. However, it has to be considered that this symmetry is

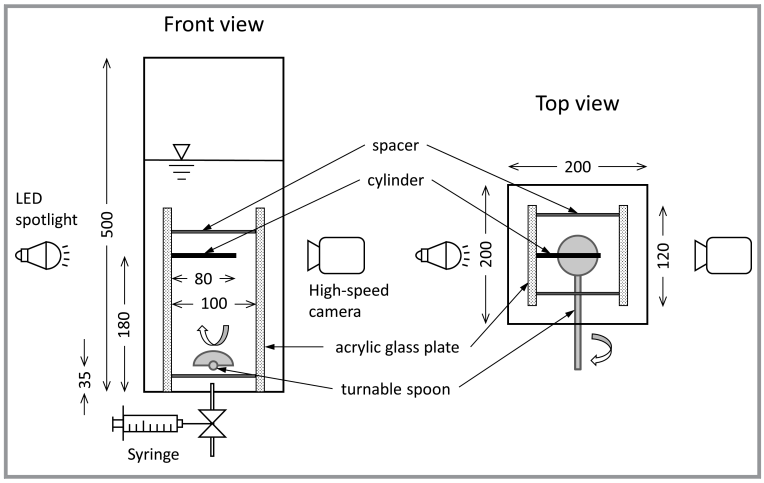

Figure 2. Experimental set up (not to scale, all dimensions in mm).

broken by the interaction with the cylinder. All cases were repeated several times.

2.3 Physical Properties

Experiments have been performed at room temperature. Physical properties of the glycerin-water mixture are estimated from literature [18–21] assuming a temperature of 20 °C. Density and viscosity are determined as $\rho_L = 1233\,\mathrm{kg\,m^{-3}}$ and $\mu_L = 0.157\,\mathrm{Pa\,s}$, respectively. Surface tension is set to $\sigma = 66\,\mathrm{mN\,m^{-1}}$. Density and viscosity of air are taken as $\rho_G = 1.2\,\mathrm{kg\,m^{-3}}$ and $\mu_G = 1.8\times10^{-5}\,\mathrm{Pa\,s}$, respectively. These physical properties result in a Morton number of $Mo = 0.0166$ while the Eötvös number (Eo) is in the range of 3.83–17.75.

3 Numerical Methodology

3.1 Governing Equations

In this paper, the diffuse interface phase-field method is used to simulate the flow of two immiscible, incompressible Newtonian fluid phases under isothermal conditions. The gas-liquid interface is considered as a thin transition layer of finite width across which density/viscosity varies rapidly yet smoothly. Phases are distinguished by an order parameter (c) which has the value $c = 1$ in the liquid phase and $c = -1$ in the gas phase. The two-phase flow is described by the coupled Cahn-Hilliard Navier-Stokes equations

$$\begin{gathered}\partial_t c + \nabla\cdot(c\mathbf{u}) = M\nabla^2\Phi\\ \Phi = \lambda\varepsilon^{-2}c(1-c^2) - \lambda\nabla^2 c\\ \nabla\cdot\mathbf{u} = 0\\ \partial_t(\rho\mathbf{u}) + \nabla\cdot(\rho\mathbf{u}\otimes\mathbf{u}) = -\nabla p + \nabla\cdot\mu\left(\nabla\mathbf{u} + (\nabla\mathbf{u})^{\mathrm{T}}\right) + \rho\mathbf{g} + \mathbf{f}_\sigma\end{gathered} \tag{1}$$

Here, M is mobility, Φ is chemical potential, λ is mixing energy density, and ε is capillary width. Furthermore, $\mathbf{u}$ is velocity field, p is pressure, and $\mathbf{g}$ is gravity vector. The density and viscosity are computed based on the order parameter using an arithmetic mean

$$\rho = \frac{1+c}{2}\rho_L + \frac{1-c}{2}\rho_G \tag{2}$$

$$\mu = \frac{1+c}{2}\mu_L + \frac{1-c}{2}\mu_G \tag{3}$$

Surface tension is modeled as $\mathbf{f}_\sigma = -c\nabla\Phi$ where mixing energy density is determined as $\lambda = 3\varepsilon\sigma/\sqrt{8}$. Cylinder wettability is accounted for by a boundary condition for the gradient of the order parameter normal to the wall

$$\mathbf{n}_{\mathrm{cyl}}\cdot\nabla c = \frac{\cos\theta}{\sqrt{2}\varepsilon}\left(1-c^2\right) \tag{4}$$

where $\mathbf{n}_{\mathrm{cyl}}$ is the unit normal vector pointing from the cylinder surface into the fluid. Simulations are performed with the physical properties given in Sect. 2.3.

The set of equations is numerically solved using OpenFOAM extend 1.6 (code phaseFieldFoam). A description of the segregated solution algorithm and applied discretization schemes is provided in [22, 23]. Method and code have been validated thoroughly. Validation examples include analytical solutions for various wetting phenomena [22], the standard test case of a bubble in static equilibrium [24], and experiments on drop impingement on hydrophobic surfaces [25].

3.2 Computational Set Up

The simulations are performed in rectangular, wedge-type, or cuboid computational domains. Boundary conditions at the sides of the computational domain (width W) are free-slip or symmetry planes in combination with zero gradient conditions for the order parameter and chemical potential. At the cylinder wall, no-slip conditions apply in combination with a prescribed equilibrium contact angle according to Eq. (4).

All simulations are started from an initially circular/spherical bubble placed in the lower part of the computational domain with both phases being at rest. In the experiment, the bubbles rise after being released by turning the spoon about 145 mm before interacting with the cylinder. In the simulations, the height of the domain (H) needs to be restricted to reduce the computational costs. On the other hand, the computational domain must be high enough to ensure that the bubble has obtained its terminal rise velocity (U_B) before interacting with the cylinder. The corresponding rising distance is determined from simulations without cylinder (see Sect. 3.3). The domain height in cases with cylinder is adapted accordingly.

3.3 Determination of Phase-Field Parameters

Remaining parameters of the phase-field method that need to be fixed are ε and M. The capillary width ε is determined indirectly by specifying a certain value of the Cahn number $Cn = \varepsilon/d_{\mathrm{eq}}$. The latter determines the thickness of the diffuse interface relative to the bubble diameter; thus, Cn should be sufficiently small to obtain accurate results comparable with more common sharp interface methods. Mobility is scaled as $M = \chi\varepsilon^2$, where χ is a pre-factor. To study the effects of Cn and χ on free bubble rise, the first one of the two planar benchmark cases proposed in [26] has been computed. Results obtained by the present phase-field method are in good agreement with the benchmark solution for $Cn \le 0.01$ and are mesh-independent for $h \le \varepsilon/2$, where h is the mesh size [27]. Thus, all simulations are performed with $Cn = 0.01$ so that $\varepsilon = 0.01 d_{\mathrm{eq}}$. For computations utilizing a uniform grid, mesh size is set here to $h = \varepsilon$ so that the

bubble diameter is resolved by 100 cells, while the diffuse interface region (where $-0.9 \le c \le 0.9$) is resolved by four mesh cells to reduce computational costs. The time step width Δt is adaptive and adjusted based on the maximum Courant number Co_{max}, which is set to 0.03 here. In addition, a criterion for the maximum time step width has been specified as $\Delta t_{max} = 1\,\mu s$.

Present numerical results for benchmark [26] show a slight influence of mobility on bubble rise velocity [27]. Such a dependency has already been noted in [15]. To determine mobility and rising height required for the bubble to reach terminal velocity, simulations for freely rising bubbles are performed in a wedge-type domain ($W = 3d_{eq}$, $H = 9d_{eq}$) assuming rotational symmetry applying a uniform grid (300×900 cells, $h = \varepsilon = 0.01 d_{eq}$). The value of χ is determined so that the numerical rise velocity agrees with U_B estimated by Eq. (13) in [28] as given in Tab. 1. Values of χ are determined for the two larger bubble volumes, while for the smallest bubble, the standard value is used (Tab. 1). The values of bubble Reynolds numbers (Re) are in the range of 3.51–14.95.

Table 1. Investigated bubble volumes and terminal velocity for free bubble rise.

V_B [µL]	d_{eq} [mm]	d_{eq}/d_{cyl} [mm]	Eo [–]	χ [m s kg^{-1}]	U_B [mm s^{-1}]	Re [–]
50	4.57	1.14	3.83	1	97.4	3.51
250	7.82	1.95	11.18	2	159.6	9.82
500	9.85	2.46	17.75	8	192.8	14.95

4 Results for Bubble Cutting

This section presents numerical results of bubble cutting simulations in 2D and 3D. Planar simulations serve for preliminary qualitative investigations, while 3D results provide a comprehensive understanding of the cutting process and allow for a detailed comparison with experiments.

4.1 Two-Dimensional Planar Simulations

The experimental bubble volumes considered for 2D computations are 50 and 250 µL in combination with the stainless steel cylinder. While the simulations are 2D, they use the equivalent diameter from the experiments (Tab. 1). The initial area of the circular bubble in simulations thus corresponds to the projected area of a spherical experimental bubble. It should be kept in mind that this initial equivalence of (projected) area is not valid as the bubble deforms from the circular/spherical shape. This is because 3D effects along the cylinder axis in the experiment are suppressed in the 2D simulations.

4.1.1 Bubble Volume 50 µL

In the experiments with 50-µL bubbles, it is observed that bubbles of this size are never split by the cylinder. Instead, they always slide-off at one side of the cylinder (Fig. 3, top). This behavior is related to the bubble release mechanism, by which it is very unlikely that the bubble centroid is located exactly below the cylinder axis. Even a very small horizontal offset between bubble centroid and cylinder axis breaks symmetry, which triggers slide-off of very small bubbles in the experiment. In the 2D simulations, the 50-µL bubble is therefore placed below the cylinder with a slight horizontal offset of 0.1 mm to replicate the behavior observed in the experiment. The rectangular computational domain ($W = 4d_{eq}$, $H = 6d_{eq}$) is discretized by a uniform grid (400×600 cells, $h = 45.7\,\mu m$).

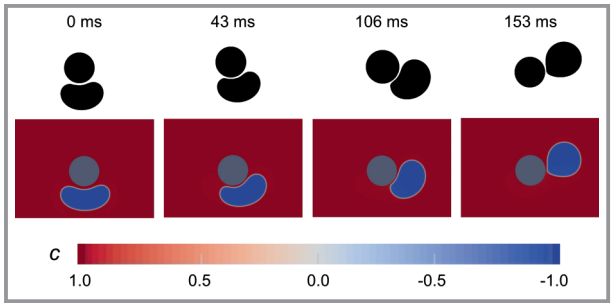

Figure 3. Evolution of bubble (50 µL) approaching a steel cylinder ($\theta = 60°$) in experiment (above) and 2D simulation (below). Simulation results show contour plots of order parameter c in a section of the computational domain. Time instants of the 2D simulation do not match with the experiment but are chosen to illustrate qualitative similarity.

The simulation results are displayed in the bottom row of Fig. 3. Though the simulations are 2D, the computed bubble shape is consistent with the experiment and results are in qualitative agreement. During the entire process, the bubble is separated from the cylinder by a thin liquid film. The thickness of the liquid film in the simulation corresponds to about 6ε.

4.1.2 Bubble Volume 250 µL

In the 2D simulations for the 250-µL bubble, the bubble center is placed exactly below the cylinder axis without offset. Only one-half of bubble/cylinder are represented in the computational domain ($W = 2.5d_{eq}$, $H = 8d_{eq}$, grid 250×800, $h = 78\,\mu m$). By a symmetry boundary condition, a splitting of the bubble is enforced in contrast to the previous case. To study the influence of cylinder wettability, simulations for contact angles of 60°, 90°, and 120° have been performed. Fig. 4 compares the results for $\theta = 60°$ and 120° and with experiment ($\theta = 40°$). As the bubble approaches the cylinder, it deforms taking a concave shape. Simulation results agree qualitatively with the experiment concerning the general bubble deformation, the formation

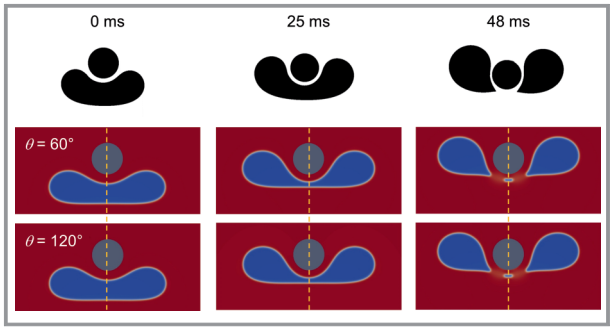

Figure 4. Evolution of a rising bubble (250 µL) approaching a cylinder (4 mm). Experiment (θ = 40°, top) and 2D simulations with θ = 60° (middle) and 120° (below). Numerical results show contour plots of c in a section of the domain (for color legend, see Fig. 3). The dashed vertical lines indicate the symmetry plane. While the time instants in simulations with both contact angles are identical, they do not match with the experiment but are chosen to illustrate similar stages of the splitting process.

of a liquid film that separates the bubble from the cylinder, and for the breakup of the mother bubble into two daughter bubbles. Both in experiment and simulations, there is no contact between gas bubble and cylinder. The presence of the liquid film eliminates any influence of cylinder wettability, so that in experiments [17] and simulations [27] there is no difference for contact angles in the range of 40°–120°.

Quantitatively, there are notable differences between 2D simulation and experiment concerning the lateral dimensions of the bubble, the thickness of the neck connecting the forming daughter bubbles before breakup, and the shape of the lower meniscus, which is almost flat in the 2D simulations while it is convex in the experiment.

4.2 Three-Dimensional Simulations

While the previous planar simulations for bubble cutting are in qualitative agreement with the experiment, they fail to give a quantitative agreement. This indicates that deformation in the direction of the cylinder axis is of importance, which requires 3D simulations.

Fig. 5 shows the computational domain for 3D simulations together with a detail of the initial mesh for a bubble volume of 500 µL. Quarter symmetry is adopted. The width/depth of the computational domain are $2.5d_{eq}$, height is $H = 12d_{cyl}$, and cylinder contact angle is 60°. The grid consists of three levels. Far from bubble and cylinder, a coarse mesh is used ($h = d_{eq}/25$, refinement level 0). In the rise path of the bubble and around the cylinder, mesh width is $h = d_{eq}/50$ (refinement level 1). In the region of the diffuse interface, mesh width is $h = \varepsilon = d_{eq}/100$ (refinement level 2) corresponding to $Cn = 0.01$. Only refinement level 2 is adaptive according to the bubble motion. With this strategy, the total number of mesh cells is about 1.5×10^6.

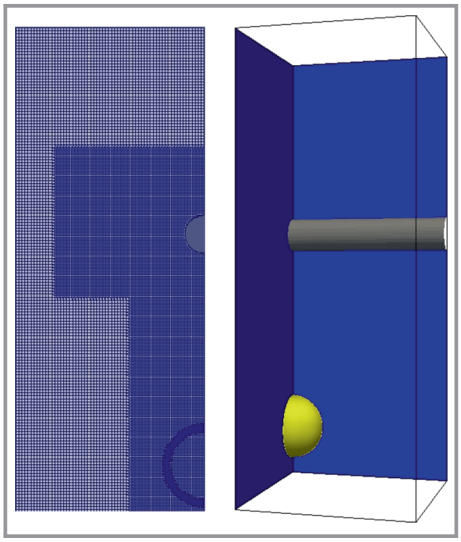

Figure 5. Computational domain for 3D simulations showing initial bubble position (right) and corresponding initial grid at symmetry plane along cylinder axis (left) for a bubble volume of 500 µL.

4.2.1 Bubble Volume 250 µL

Fig. 6 shows the interface evolution for the 250-µL bubble during the cutting process in 3D. In the front view, the computed bubble shape (Fig. 6, top) shows better match with the experiment (Fig. 4, top) as compared to the 2D simulations. Two major improvements can be noted. First, the bubble deformation before breakup is well in accordance with the experiment instead of the lateral over-extension found in 2D. Second, the lower meniscus of the bubble is convex, whereas it was flat in the planar case. Despite these improvements, the split process in the simulation takes notably longer as compared to the experiment.

In the simulation view from below, the generation and evolution of the neck can be observed (Fig. 6, bottom). Over time, the neck shrinks in vertical direction and in direction of the cylinder axis, forming a thin gas thread. Finally, the thread breaks and two daughter bubbles are formed which quickly adopt almost spherical shapes under influence of surface tension. From the gas thread, a satellite bubble is formed in the simulation which is absent in the experiment. Similar satellite bubbles have been observed in simulations with the volume-of-fluid method [13, 14]. Possible reasons for the discrepancy in satellite bubbles in experiment and simulations are discussed in Sect. 4.2.3.

4.2.2 Bubble Volume 500 µL

The cutting process for the 500-µL bubble is illustrated in Fig. 7. The computed shapes of the mother and daughter bubbles in front view (Fig. 7, middle) and the duration of the split process are well in accordance with the experiment (Fig. 7, top). Compared with the smaller bubble, the 500-µL

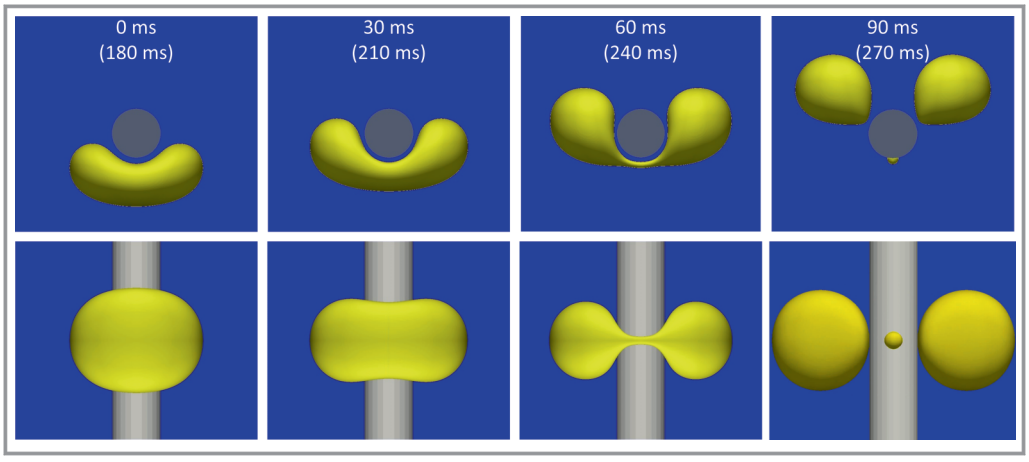

Figure 6. Simulation results (3D) for cutting of 250 µL bubble with views from front (above) and bottom (below). Corresponding experimental results are shown in the top row of Fig. 4. Indicated simulation times have an offset of 180 ms compared to the first experimental image. The actual simulation times are given in brackets.

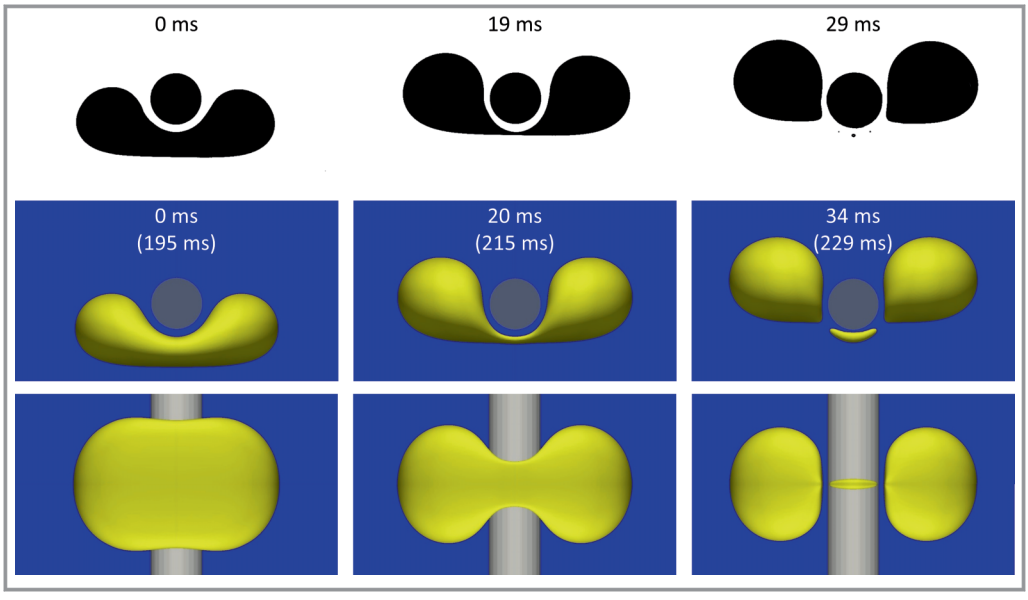

Figure 7. Cutting of 500 µL bubble in experiment (top) and 3D simulation (middle and below). Views are from front (top and middle) and bottom (below). Indicated simulation times have an offset of 195 ms compared to the first experimental image. The actual simulation times are given in brackets.

bubble undergoes stronger deformation before the breakup due to higher Eötvös number, while the cutting process is actually very similar for both bubble volumes. The 500-µL bubble also shrinks quickly in the middle, whereas no significant deformation can be observed on the left and right sides. Again, the cylinder stays completely wetted in experiment and simulation so that neither the behavior of mother nor daughter bubbles is affected by surface wettability. However, though not shown here, cylinder contact angle may affect the behavior of satellite bubbles as they adhere to the surface [17].

4.2.3 Satellite Bubbles

Satellite bubbles show the largest difference between simulation and experiment. In the experiment for a bubble volume of 500 µL, three satellite bubbles are formed (Fig. 7, top), while no satellite bubble is formed for a volume of 250 µL (Fig. 4, top). It should be noted that in the experiment, the number of satellite bubbles varies and is not always reproducible, especially for larger bubbles. In the simulations, one satellite bubble is formed for each considered bubble volume. The 3D simulations clearly reveal that the mechanism for formation of satellite bubbles is the breakup of the thinning gas thread. However, the simulation fails to correctly predict the occurrence of satellite bubbles and their number and sizes. The reason lies in the thickness of the diffusive interface which is chosen here as $\varepsilon = 0.01 d_{eq}$. For computation of satellite bubbles with the phase-field method, the relevant macroscopic length scale is, however, not the equivalent bubble diameter but the diameter of the gas thread. Thus, ε should be reduced by one order of magnitude or more, which is out of reach for our method currently even with adaptive mesh refinement. Another computational challenge for numerical methods is the extreme curvature of the cusp immediately after breakup of the gas thread observed in the experiment [17].

4.2.4 Thickness of the Separating Liquid Film

As discussed before, the presence of the liquid film that separates the gas from the cylinder surface effectively eliminates the influence of surface wettability on the bubble cutting process. This finding is supported by experimental visualizations for further contact angles (with a range of about 40°–150°) which cannot be displayed here for the sake of brevity [17]. The liquid film around the lower hemisphere of the cylinder is rather uniform and its thickness is constant over a duration of about 50–100 ms. Fig. 8 shows the thickness of the liquid film (measured vertically below the cylinder) as a function of bubble volume. For volumes of 250 and 500 µL, reasonable agreement is achieved between simulation and experiment. In addition to these two bubble volumes, experimental results for further bubble sizes from [17] are included in Fig. 8, which have not been simulated here. The results indicate that the thickness of the separating liquid film increases with increase of bubble volume. Splitting of bubbles in experiments is only observed if the volume exceeds about 100 µL, while smaller bubbles always slide off.

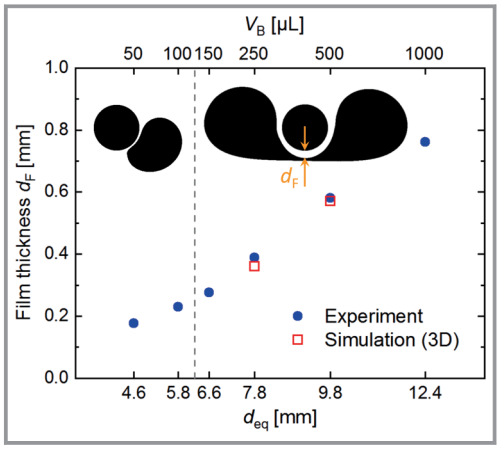

Figure 8. Thickness of liquid film (d_F) separating bubble and cylinder (4 mm) versus bubble volume. The dashed vertical line discriminates between slide-off (left) and bubble-cutting (right) as observed in the experiment.

The thickness of the liquid film in the present simulations with Cn = 0.01 is about 5 to 6 times the capillary width, while the thickness of the diffuse interface is about 4ε. Cai et al. [15] performed their calculations with Cn = 0.02 corresponding to double interface width. This was obviously insufficient to resolve the liquid film so that a wettability-dependent interaction of bubbles with the cylinder and periodic open cell structures was observed, which might be actually a numerical artifact.

5 Conclusions

Experiments are performed to study the splitting of single bubbles rising in a viscous liquid by horizontal cylinders. They are supported by numerical simulations with a diffuse interface phase-field method based on the coupled Cahn-Hilliard Navier-Stokes equations covering a wide range of cylinder wettability. Overall, numerical and experimental results are in good agreement. They consistently show that during the splitting process, bubbles do not come in direct contact with the cylinder. Instead, a separating liquid film is formed which eliminates any effect of surface wettability. Notably, the film thickness increases with bubble volume. Simulations show the formation of a thinning gas thread below the cylinder, which may break up with or without generation of satellite bubbles. Correct capturing of these tiny satellite bubbles is currently out of reach with the phase-field method, as it requires a reduction of the diffuse interface thickness by an order of magnitude as compared to the value used here.

For three-phase reactions, enhanced gas-liquid mass transfer and short diffusion path of dissolved educts toward the catalytic surface are of interest. The present results show that the diffusion path between the bubble and the catalyst support given by the liquid film notably increases with bubble volume despite increase of bubble rise velocity. This finding substantiates that reduction of bubble size is essential to intensify three-phase reactions at least in very viscous liquids as considered here.

Supporting Information

Supporting Information for this article can be found under DOI: https://doi.org/10.1002/cite.202100145.

M. Börnhorst, H. Marschall, O. Deutschmann, and M. Wörner acknowledge support by DFG through project 237267381 – TRR 150. Special thanks go to J. Kriegseis and B. Frohnapfel (KIT, ISTM) for providing high-speed camera equipment and to H. Weickenmeier for support with the experimental set up. Computations were performed on bwUniCluster funded by the state of Baden-Württemberg through bwHPC. Open access funding enabled and organized by Projekt DEAL.

Symbols used

c	[–]	order parameter
Cn	[–]	Cahn number, ε/d_{eq}
Co	[–]	Courant number, $\Delta t \lvert \mathbf{u} \rvert /h$
d_{cyl}	[m]	cylinder diameter

d_{eq}	[m]	volume-equivalent bubble diameter, $(6V_B/\pi)^{1/3}$
d_F	[m]	liquid film thickness
Eo	[–]	Eötvös number, $g(\rho_L - \rho_G)d_{eq}^2/\sigma$
$\mathbf{f}_\sigma$	[N m^{-3}]	surface tension force
g	[m s^{-2}]	gravitational acceleration, 9.81
h	[m]	mesh size
H	[m]	height of computational domain
M	[m^{3}s kg^{-1}]	mobility
Mo	[–]	Morton number, $(\rho_L - \rho_G)g\mu_L^4/(\sigma^3\rho_L^2)$
$\mathbf{n}_{cyl}$	[–]	unit normal vector to cylinder surface
p	[N m^{-2}]	pressure
Re	[–]	Reynolds number, $\rho_L d_{eq} U_B/\mu_L$
t	[s]	time
Δt	[s]	time step width
$\mathbf{u}$	[m s^{-1}]	velocity field
U_B	[m s^{-1}]	terminal bubble rise velocity
V_B	[µL]	bubble volume
W	[m]	width of computational domain

Greek letters

ε	[m]	capillary width
θ	[°]	contact angle
λ	[J m^{-1}]	mixing energy density
μ	[Pa s]	dynamic viscosity
ρ	[kg m^{-3}]	density
σ	[N m^{-1}]	coefficient of surface tension
Φ	[J m^{-3}]	chemical potential
χ	[m s kg^{-1}]	mobility pre-factor

Subscripts

B	bubble
cyl	cylinder
F	film
G	gas
L	liquid

References

[1] R. Ulber, D. Sell, T. Hirth, *Renewable Raw Materials – New Feedstocks for the Chemical Industry*, Wiley-VCH, Weinheim **2011**.

[2] N. Dahmen et al., *Environ. Prog. Sustainable Energy* **2012**, *31 (2)*, 176–181. DOI: https://doi.org/10.1002/ep.10624

[3] C. B. Vik, J. Solsvik, M. Hillestad, H. A. Jakobsen, *Chem. Eng. Technol.* **2015**, *38 (4)*, 690–700. DOI: https://doi.org/10.1002/ceat.201400647

[4] A. A. Youssef, M. H. Al-Dahhan, M. P. Dudukovic, *Int. J. Chem. React. Eng.* **2013**, *11 (1)*, 169–223. DOI: https://doi.org/10.1515/ijcre-2012-0023

[5] F. Möller et al., *Chem. Ing. Tech.* **2019**, *91 (9)*, 1339–1346. DOI: https://doi.org/10.1002/cite.201800110

[6] V. Höller et al., *Chem. Eng. Technol.* **2000**, *23 (3)*, 251–255. DOI: https://doi.org/10.1002/(SICI)1521-4125(200003)23:3<251::AID-CEAT251>3.0.CO;2-S

[7] V. Höller, K. Radevik, L. Kiwi-Minsker, A. Renken, *Ind. Eng. Chem. Res.* **2001**, *40 (6)*, 1575–1579. DOI: https://doi.org/10.1021/ie000719f

[8] L. Kiwi-Minsker, I. Yuranov, V. Höller, A. Renken, *Chem. Eng. Sci.* **1999**, *54 (21)*, 4785–4790. DOI: https://doi.org/10.1016/S0009-2509(99)00195-5

[9] M. W. Baltussen, J. A. M. Kuipers, N. G. Deen, *Chem. Eng. Sci.* **2017**, *165*, 25–32. DOI: https://doi.org/10.1016/j.ces.2017.01.037

[10] D. Jain, Y. M. Lau, J. A. M. Kuipers, N. G. Deen, *Chem. Eng. Sci.* **2013**, *100*, 496–505. DOI: https://doi.org/10.1016/j.ces.2013.02.060

[11] K. T. Sujatha et al., *Chem. Eng. Sci.* **2017**, *169*, 225–234. DOI: https://doi.org/10.1016/j.ces.2016.12.035

[12] K. T. Sujatha, B. G. J. Meeusen, J. A. M. Kuipers, N. G. Deen, *Chem. Eng. Sci.* **2015**, *130*, 18–30. DOI: https://doi.org/10.1016/j.ces.2015.02.029

[13] Q. I. E. Segers, Cutting Bubbles Using Wire-Mesh Structures – Direct Numerical Simulations, *Proefschrift*, Technische Universiteit Eindhoven **2015**.

[14] M. W. Baltussen, Q. I. E. Segers, J. A. M. Kuipers, N. G. Deen, *Chem. Eng. Sci.* **2017**, *157*, 138–146. DOI: https://doi.org/10.1016/j.ces.2016.04.052

[15] X. Cai, M. Wörner, H. Marschall, O. Deutschmann, *Catal. Today* **2016**, *273*, 151–160. DOI: https://doi.org/10.1016/j.cattod.2016.03.053

[16] R. Park, W. Kim, *Int. J. Multiphase Flow* **2019**, *118*, 165–172. DOI: https://doi.org/10.1016/j.ijmultiphaseflow.2019.06.016

[17] P. Rohlfs, Einfluss des Benetzungsverhaltens auf die Blasenzerteilung an einem Zylinder, *Bachelor Thesis*, Karlsruhe Institute of Technology **2018**. DOI: https://doi.org/10.5445/IR/1000135666

[18] N.-S. Cheng, *Ind. Eng. Chem. Res.* **2008**, *47 (9)*, 3285–3288. DOI: https://doi.org/10.1021/ie071349z

[19] K. Takamura, H. Fischer, N. R. Morrow, *J. Pet. Sci. Eng.* **2012**, *98–99*, 50–60. DOI: https://doi.org/10.1016/j.petrol.2012.09.003

[20] L. Liu, H. J. Yan, G. J. Zhao, J. C. Zhuang, *Exp. Therm. Fluid Sci.* **2016**, *78*, 254–265. DOI: https://doi.org/10.1016/j.expthermflusci.2016.06.011

[21] A. Volk, C. J. Kähler, *Exp. Fluids* **2018**, *59 (5)*, 75. DOI: https://doi.org/10.1007/s00348-018-2527-y

[22] X. Cai, H. Marschall, M. Wörner, O. Deutschmann, *Chem. Eng. Technol.* **2015**, *38 (11)*, 1985–1992. DOI: https://doi.org/10.1002/ceat.201500089

[23] X. Cai, M. Wörner, H. Marschall, O. Deutschmann, *Emiss. Control Sci. Technol.* **2017**, *3 (4)*, 289–301. DOI: https://doi.org/10.1007/s40825-017-0073-3

[24] F. Jamshidi et al., *Comput. Phys. Commun.* **2019**, *236*, 72–85. DOI: https://doi.org/10.1016/j.cpc.2018.10.015

[25] V. Fink et al., *Int. J. Heat Fluid Flow* **2018**, *70*, 271–278. DOI: https://doi.org/10.1016/j.ijheatfluidflow.2018.02.014

[26] S. Hysing et al., *Int. J. Numer. Methods Fluids* **2009**, *60 (11)*, 1259–1288. DOI: https://doi.org/10.1002/fld.1934

[27] S. Wang, Numerical Simulation of the Cutting of a Rising Bubble by a Horizontal Cylinder, *Master Thesis*, Karlsruhe Institute of Technology **2019**. DOI: https://doi.org/10.5445/IR/1000135974

[28] S. H. Park, C. Park, J. Lee, B. Lee, *Nucl. Eng. Technol.* **2017**, *49 (4)*, 692–699. DOI: https://doi.org/10.1016/j.net.2016.12.006

